Efficient Oxygen Evolution Electrocatalyst by Incorporation of Nickel into Nanoscale Dicobalt Boride

Jona Schuch[+],*[a] Sebastian Klemenz[+],[b] Patrick Schuldt,[a] Anne-Marie Zieschang,[b] Stephanie Dolique,[b] Paula Connor,[a] Bernhard Kaiser,[a] Ulrike I. Kramm,[c] Barbara Albert,[b] and Wolfram Jaegermann[a]

Recently, transition metal borides attracted increased attention as electrocatalysts for the oxygen evolution reaction. Here, we show how the incorporation of nickel into nanoscale dicobalt boride results in an improvement of the activity and stability of the catalyst in alkaline electrolytes. The borides are obtained by a one-step solution synthesis, calcined, and characterized by X-ray diffraction and scanning electron microscopy. For $(Co_{1-x}Ni_x)_2B$ (x = 0, 0.1, 0.2, 0.3, 0.4, and 0.5), $(Co_{0.9}Ni_{0.1})_2B$ shows the best performance with an overpotential of $\eta = 371$ mV at 10 mA cm^{-2} in 1 M KOH. Normalization to the electrochemical surface area shows a clear dependence on the activity with rising nickel content. X-ray photoelectron spectroscopy reveals that the catalyst is modified under reaction conditions and indicates that CoOOH and $Ni(OH)_2$ are formed as active surface species. Flame atomic absorption spectroscopy (F-AAS) measurements show that no cobalt is dissolved during the electrochemical investigations, but the nickel concentration is increased on the surface of the catalyst as follows from XPS measurements after the electrochemical investigation.

Introduction

Metal borides are a structurally complex group of compounds with interesting properties and potential applications.[1] It is well-known that borides are impressive refractory materials for high-temperature applications,[1–4] but their functional properties e.g. for magnetism and catalysis are less explored.[1,5–7] Osaka et al. observed in 1980 that certain transition metal borides were active electrocatalysts for the oxygen evolution reaction (OER).[8,9] Recently, binary metal borides with Co,[10–16] Fe,[12,15,17–19] and Ni,[11,12,14,19–21] were found to show high catalytic efficiencies for the OER. A recent review on the application of metal borides as electrocatalyst is given by Gupta et al.[7] From previous research concerning 3d-metal oxides it is known that a mixture of at least two metals can improve the overall catalytic performance of the material.[22–26] This is due to the invalid scaling relation as stated by Halck et al.[27] However, the reaction mechanism and the synergetic effects of bimetallic systems are still a research focus.[7] There are only a few systematic studies about the incorporation of a second transition metal into binary boride OER catalysts, as these incorporation limits for transition metal oxides have been researched intensively.[22,28,29] For Ni–Fe oxide systems, Friebel et al.[28] proposed that the incorporation of 25% of iron shows the maximum improvement for the OER activity. They stated that the iron centers act as the active site, whereas the nickel mainly improves the overall conductivity of the catalyst. For Co–Fe oxide systems similar results were found with an enhancement in intrinsic activity by a factor of 100 as shown by Burke et al..[22] It was suggested that FeOOH provides the active centers and CoOOH stabilizes the iron compound in the alkaline electrolyte by forming a stable matrix.[22] For Co–Ni oxide catalysts, Li et al.[29] showed that the electric conductivity of nanowires of Co_3O_4 was increased by a factor of two due to an incorporation of nickel caused by a larger number of accessible active sites.

Due to the fact that metal borides (M_2B) usually have a higher electrical conductivity than metal oxides,[5,30] and are often forming metal oxyhydroxide active surface species in ambient conditions or alkaline electrolytes,[10,13,21,31] the next step should be to systematically investigate mixed-metal borides (Ni, Co, Fe) with defined amounts of incorporated metal phases, in order to find and identify new promising electrocatalysts for OER. In one of our previous studies we found that the incorporation of iron into nanoscale dicobalt boride $(Co_{1-x}Fe_x)_2B$ not only led to a reduction in the onset potential by about 100 mV, but also increased the overall activity and

[a] J. Schuch,[+] P. Schuldt, Dr. P. Connor, Dr. B. Kaiser, Prof. W. Jaegermann
Institute of Materials Science, Surface Science Division
Technical University of Darmstadt
Otto-Berndt-Str. 3
64287 Darmstadt (Germany)
E-mail: jschuch@surface.tu-darmstadt.de
[b] Dr. S. Klemenz,[+] Dr. A.-M. Zieschang, S. Dolique, B. Albert
Department of Chemistry
Eduard-Zintl-Institute of Inorganic and Physical Chemistry
Technical University of Darmstadt
Alarich-Weiss-Str. 12
64287 Darmstadt (Germany)
[c] Prof. U. I. Kramm
Institute of Materials Science and Department of Chemistry
Catalysts and Electrocatalysts group
Technical University of Darmstadt
Otto-Berndt-Str. 3
64287 Darmstadt (Germany)
[+] These authors contributed equally to this project and should be considered co-first authors.

Supporting information for this article is available on the WWW under https://doi.org/10.1002/cctc.202002030

© 2021 The Authors. ChemCatChem published by Wiley-VCH GmbH. This is an open access article under the terms of the Creative Commons Attribution License, which permits use, distribution and reproduction in any medium, provided the original work is properly cited.

stability of the catalyst.[13] The previously described low-temperature synthesis method[13] was used in this work to form amorphous Co–Ni–B pre-catalysts. After annealing at moderate temperatures, a crystalline material resulted that consisted mostly of $(Co_{1-x}Ni_x)_2B$ (x = 0, 0.1, 0.2, 0.3, 0.4, and 0.5). The mixed-metal boride nano-powders were characterized by X-ray diffraction (XRD), scanning electron microscopy (SEM), transition electron microscopy (TEM) and energy dispersive X-ray spectroscopy (EDX) to confirm their phase compositions and particle sizes. X-ray photoelectron spectroscopy (XPS) was used to detect and analyze surface species and monitor changes in the catalysts after electrochemical reactions. Flame atomic absorption spectroscopy (F-AAS) was used to investigate the metal content of the alkaline electrolyte to check for dissolution of metal species from the catalysts.

Experimental section

Synthesis of nanoscale $(Co_{1-x}Ni_x)_2B$

Nanoscale mixed-metal borides were synthesized following a previously published method.[13] The amounts of the starting materials, cobalt(II) chloride hexahydrate (97%, VWR) and nickel(II) chloride hexahydrate (98%, Riedel-de Haën), were calculated for 1 g $NaBH_4$ (>97%, Alfa Aeser) to obtain a molar ratio of tetrahydridoborate-to-metal ions of 4:1. The following steps were performed in argon atmosphere. Sodium tetrahydridoborate was dissolved in 100 ml of degassed water and slowly added dropwise to a solution of the metal chlorides in 150 ml of degassed water. Immediately, a black product precipitated from the solution and gas evolution was observed. The reaction mixture was stirred at room temperature for one hour. The precipitate was separated and washed with 50 ml of degassed water and 100 ml of dry acetone. After drying in vacuo the precipitate was transferred into a Schlenk tube and annealed in vacuo for two hours at 500 °C.

Electrode assembly

5 mg of the $(Co_{1-x}Ni_x)_2B$ catalyst powder were added to a mixture of 450 µL ethanol, 450 µL ultra-pure distilled water (Water purifier by Merck – Millipore Milli-Q®) and 100 µL Nafion (5 wt% – Aldrich). The ink was then blended using an ultrasonic bath for at least 30 minutes. Glassy carbon (HTW GmbH) was used as substrate material, sanded with abrasive paper (400, 1000, 1500, 2000, 2500 grit size, Starcke) and polished with Al_2O_3 paste (1 µm, 0.05 µm grit size, Buehler). Before application of the ink, the substrate was cleaned in an ultrasonic bath with acetone, isopropanol and ultra-pure distilled water for ten minutes each. 15 µL of the ink were loaded onto the glassy carbon substrate with an Eppendorf pipette and dried for at least 30 minutes under ambient conditions. The area of the deposited catalyst drop is 0.5 cm^2, resulting in a loading of 150 $\mu g\,cm^{-2}$. For the EC experiments, the electrode area is lowered to 0.2 cm^2 as an O-ring of the corresponding diameter (d = 0.5 cm) was used for sealing. Thus, only 30 µg of the catalyst are in electrolyte contact.

Pre-catalyst characterization

Nanoscale powders were annealed at 500 °C in vacuo. X-ray diffraction patterns were collected on a powder diffractometer (Stadi-P, Stoe) using Mo-$K_{\alpha1}$ radiation. The pattern analysis was done using the program TOPAS (version 4.2, Bruker AXS) with TCHZ-type pseudo-Voigt functions (see Supporting Information – SI; Figure S1 and Table S1). SEM images were recorded using a XL30 FEG scanning electron microscope (Philips) with an acceleration voltage of 10 kV. TEM and STEM characterization was performed on a JEOL ARM-200F operated at 200 kV acceleration voltage with a JEOL JED-2300T EDX detector (see SI – Figure S8).

Catalyst characterization

The catalytic performance tests with respect to OER were conducted using a GAMRY Interface 1000E potentiostat in a three-electrode setup with a Hg/HgO (1 M NaOH) reference electrode in 1 M KOH (Carl Roth) solution. The catalysts were first activated using cyclic voltammetry (CV) between 1 V and 1.5 V with a scan rate of 100 $mV\,s^{-1}$ until no further shifts were observable in the voltammograms. The activity was then obtained by a further CV measurement between 1 V and 1.9 V with a scan rate of 10 $mV\,s^{-1}$. Electrochemical impedance spectroscopy (EIS; 100 kHz – 100 Hz) was used to obtain the setup resistance for iR compensation. The potential sweep curve measurements (see SI; Figure S6) were conducted using a scan rate of 10, 20, 30, 40 and 50 $mV\,s^{-1}$. In this work, all electrochemical plots are calibrated to the reversible hydrogen electrode (RHE).

XPS measurements were performed with monochromatic Al-K_α radiation (XR 50, SPECS Surface Nano Analysis GmbH). A hemispherical electron analyzer (PHOIBOS 150, SPECS Surface Nano Analysis GmbH) was used, calibrated with the core lines of copper, silver, and gold. Peaks were fitted using a Shirley background.[32] Prior to the electrochemical measurements, samples of $(Co_{1-x}Ni_x)_2B$ were embedded in indium foil.

Electrolyte characterization

F-AAS measurements of the electrolyte were performed after different stages of electrolysis with a Perkin Elmer Analyst 300 using the corresponding single element hollow-cathode lamps of the elements cobalt (Agilent) and nickel (Oriel). As operating gasses acetylene and air were used. As calibrating solutions, 1 $g\,L^{-1}$ cobalt (Merck) and nickel (Carl Roth) standard solutions were used.

Results and discussion

Crystal structure, morphology, and composition

Dimetal borides Co_2B[33] and Ni_2B[34] both crystallize in a Au_2Cu-type structure (s.g. *I*4/*mcm*) with lattice parameters $a = 5.014$ Å and 4.9920 Å and $c = 4.215$ Å and 4.2465 Å, respectively. The smaller differences in lattice parameters between Co_2B and Ni_2B compared to Co_2B and Fe_2B ($a = 5.1059$ Å and $c = 4.2509$ Å)[35] make it difficult to use Vegard's law for the exact determination of the metal ratio in nanoscale mixed-metal borides. However, no sign of a phase separation into Co_2B and Ni_2B was detected and based on previous results with iron incorporation an incorporation of nickel into Co_2B can be assumed.[13] With more nickel(II) cations added to the reaction solution, Ni_3B as an additional crystalline by-product was observed (x > 0.2, cementite-type structure, s.g. *Pnma*).

The accessible surface area of a catalyst strongly influences the overall performance and can be obtained through different

© 2021 The Authors. ChemCatChem published by Wiley-VCH GmbH

measurement techniques. Firstly, SEM images of the mixed-metal borides $(Co_{1-x}Ni_x)_2B$ with different nickel contents were collected. In Figure 1 a porous morphology formed from rod-like structures in nm dimensions can be observed for all samples of the mixed-metal borides. However, the detailed structure of the different phases changes clearly. While the morphology of the pure Co_2B shows a high content of an agglomerated phase with a particle-structure, the morphology of the metal borides containing nickel reveals a more network-like structure of small rods. The samples with 10, 20 and 50% nickel content show a more porous morphology with large pores, while the sample with 30% nickel shows a less porous structure. The morphology of the $(Co_{0.6}Ni_{0.4})_2B$ exhibits in parts a particle-like structure and a porous rod-like structure with average-sized pores.

Since all samples show a similar morphology and SEM images are not able to give information about the real active area of the catalyst, a second measurement technique was used to further quantify the electrochemical "active" surface area (ECSA). This quantification will be discussed later.[36,37] Firstly, the surface of the $(Co_{1-x}Ni_x)_2B$ catalysts was investigated by XPS. Here, the XPS results of $(Co_{0.9}Ni_{0.1})_2B$ are shown exemplarily for the different measurement stages in Figure 2. The XPS measurements of the other cobalt nickel boride phases are depicted in the SI (Figure S4). The Co 2p photoemission line of $(Co_{0.9}Ni_{0.1})_2B$ before EC investigation is illustrated in Figure 2a, showing a sharp peak at 778.3 eV and several broader signals between 780 and 790 eV. The former sharp peak corresponds to Co^0, which has been observed for cobalt boride before,[38,39] while the broader signals correspond to oxidation (CoO) and hydroxylation ($Co(OH)_2$) of cobalt in the cobalt-nickel boride phase.[40–42] Similar results were found in previous studies of cobalt borides,[10,43,44] cobalt nickel borides,[45,46] and cobalt iron borides.[13,17] In contrast to the Co 2p line, the 2p photoemission line of Ni is difficult to observe (Figure 2c). A small signal at around 852.9 eV and a second contribution between 855 and 860 eV are barely visible. The first signal was assigned to Ni^0 in metal borides,[47–49] while the contribution between 855 and 860 eV corresponds mainly to hydroxylated nickel from cobalt nickel borides.[50,51] The percentage of cobalt and nickel at the surface was determined from the XPS data, using tabulated sensitivities for the experimental setup.[52] The ratios given in Table 1 are in good agreement with the assumed metal-to-metal ratios from the synthesis compositions. Furthermore, the

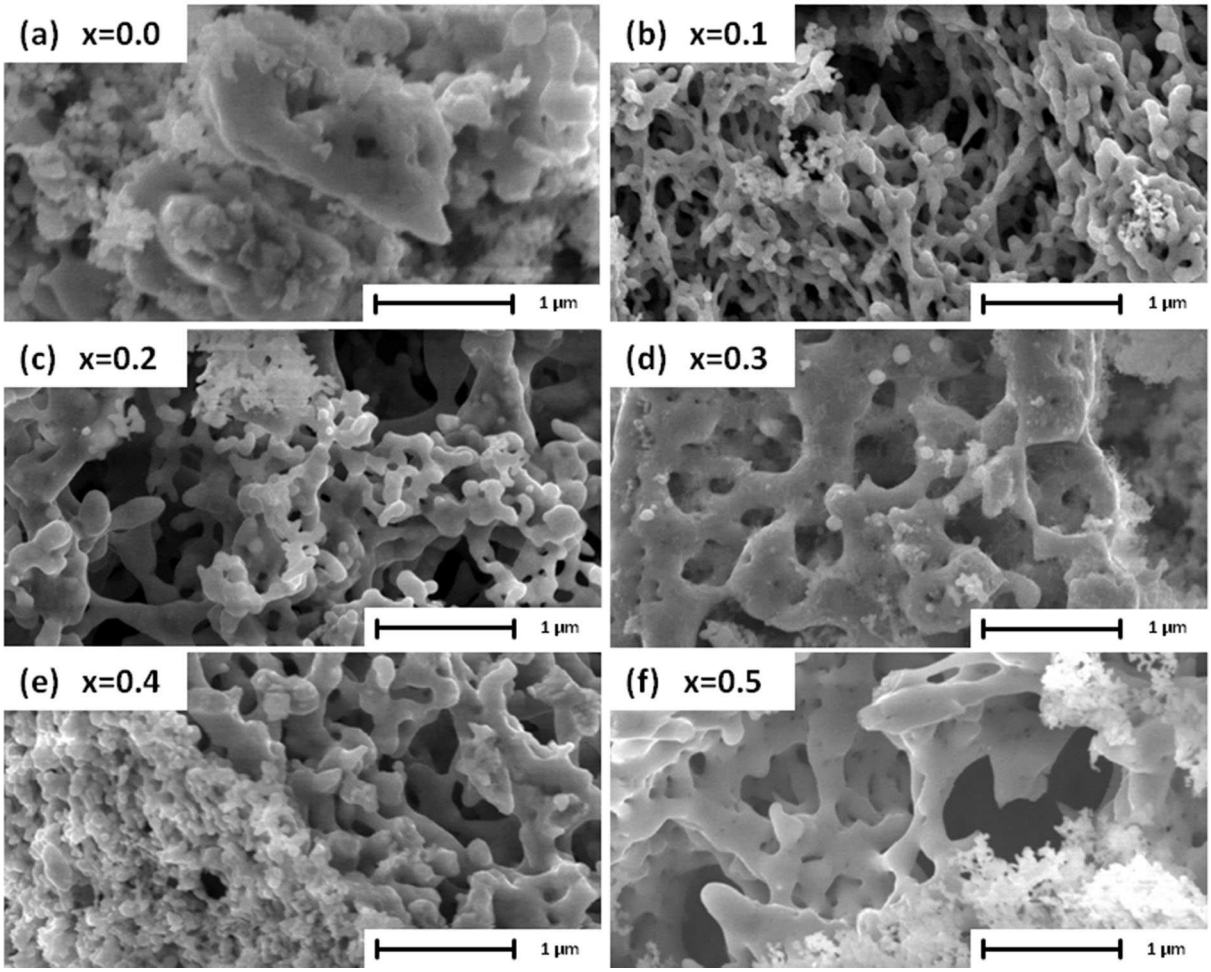

Figure 1. Scanning electron microscopy images of $(Co_{1-x}Ni_x)_2B$ with $0 \leq x \leq 0.5$.

© 2021 The Authors. ChemCatChem published by Wiley-VCH GmbH

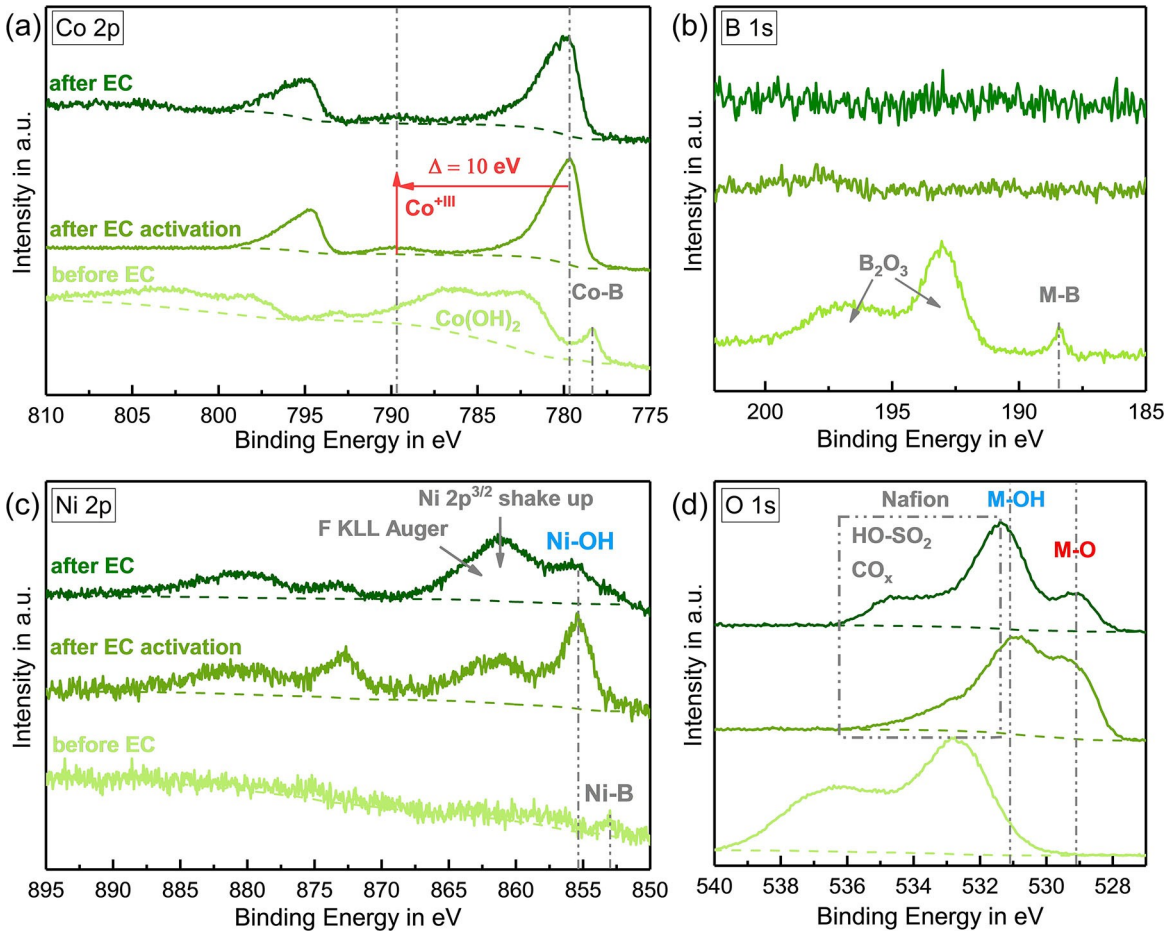

Figure 2. Co 2p (a), B 1s (b), Ni 2p (c) and O 1s (d) XPS photoemission lines of $(Co_{0.9}Ni_{0.1})_2B$ in indium foil before the electrochemical investigation (light green), after the electrochemical activation procedure (green) and after the electrochemical testing (dark green).

Table 1. Ratios of nickel-to-cobalt and boron-to-metal calculated from the synthesis parameters for the bulk and from the XPS data for the surface composition.

$(Co_{0.9}Ni_{0.1})_2B$	Synthesis bulk ratio Ni:Co	B:M	XPS surface ratio Ni:Co	B:M
before electrochemistry	0.10	0.50	0.16	0.40
after activation	–	–	0.27	0.00
after electrochemistry	–	–	0.38	0.00

boron-to-metal ratio was determined to be around 0.40, which fits quite well to the assumed composition, as the surface of the material is already oxidized to a certain degree (see TEM in SI – Figure S8). The B 1s spectrum illustrated in Figure 2b features three signals at binding energies of 188.4 eV, 193.0 eV and at 196.9 eV. The first signal contributes to the metal boride phase,[38,39,47–49] while the signals at higher binding energies correspond to oxidized boron phases boron oxides or H_3BO_3.[38,49,53–56] In the O 1s spectrum two broad peaks at around 532.5 eV and 536.1 eV were observed (Figure 2d), which can be assigned to metal hydroxides[40–42] and boron oxo-species, respectively.[53–56] Additional features at higher binding energies are attributed to oxocarbon compounds and adsorbed water.[57]

Electrochemical characterization

The electrochemical behavior of Co_2B and $(Co_{1-x}Ni_x)_2B$ ($0 \leq x \leq 0.5$) towards OER was investigated in 1 M KOH, using glassy carbon as the substrate material. It is known from literature that cobalt features an oxidation wave around 1.0–1.3 V vs. RHE, relating to $Co(OH)_2 + OH^- \rightarrow CoOOH + H_2O + e^-$.[58] An even more pronounced oxidation wave can be found for compounds containing nickel. The oxidation wave for $Ni(OH)_2 + OH^- \rightarrow NiOOH + H_2O + e^-$ is situated around 1.4–1.5 V vs. RHE.[58] Thus, the electrocatalysts were first activated by cycling between 1.0 V and 1.5 V, before measuring the final catalytic activity. The cyclic voltammograms of $(Co_{1-x}Ni_x)_2B$ after the activation procedure are presented in Figure 3a. The inset shows the shift

© 2021 The Authors. ChemCatChem published by Wiley-VCH GmbH

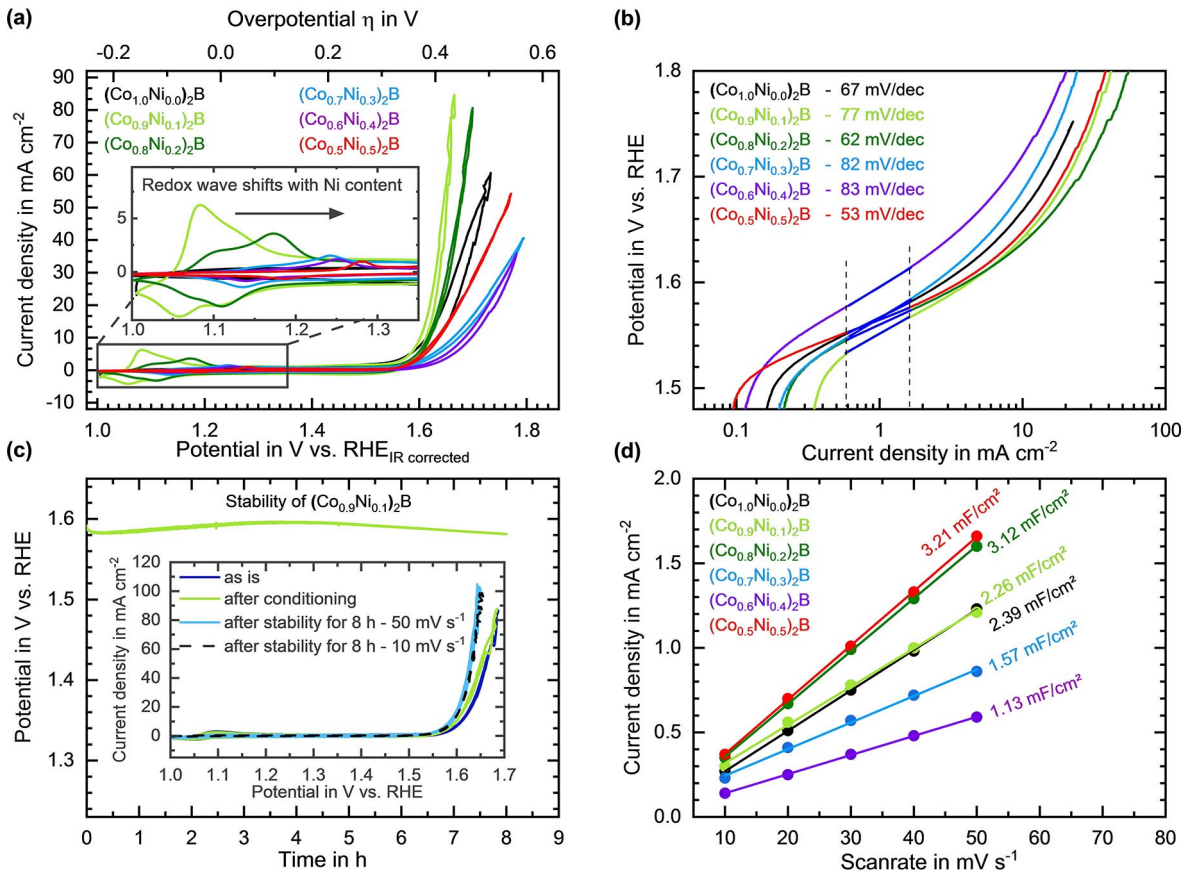

Figure 3. Electrochemical measurements in 1 M KOH electrolyte solution showing (a) cyclic voltammograms of $(Co_{1-x}Ni_x)_2B$ with $0 \leq x \leq 0.5$ with a magnification of the redox-wave shift due to the increased nickel content. The potentials are iR compensated. In (b) Tafel plots of the $(Co_{1-x}Ni_x)_2B$ are evaluated. In (d) the results of the evaluated fast sweep (cycled between 1.2 and 1.5 V vs. RHE – see SI Figure S7) curves of all $(Co_{1-x}Ni_x)_2B$ are shown, while (c) demonstrates the stability of the catalyst with a galvanostatic scan at 10 mA cm^{-2} – the inset illustrates the cyclic voltammetry behavior of different electrochemical measurement stages of $(Co_{0.9}Ni_{0.1})_2B$, before conditioning (dark blue), after conditioning (light green), and after the stability measurement (light blue and dashed black).

of the oxidation wave to higher potential with increasing nickel content.

In one of our previous studies, we found that the incorporation of iron into the binary cobalt boride decreased the onset potential towards the OER to a large extent.[13] A similar improvement cannot be observed for the incorporation of nickel into the binary cobalt boride phase. However, the incorporation of a certain amount of nickel ($x \leq 0.2$) improves the overall catalytic performance of the $(Co_{1-x}Ni_x)_2B$ catalyst. $(Co_{0.9}Ni_{0.1})_2B$ shows the best activity towards the OER with an overpotential of $\eta = 371$ mV at a current density of 10 mA cm^{-2}, followed by the $(Co_{0.8}Ni_{0.2})_2B$ catalyst with an overpotential of $\eta = 383$ mV at a current density of 10 mA cm^{-2}. A higher amount of nickel incorporation ($0.3 \leq x \leq 0.5$) reduces the electrochemical performance with respect to the binary cobalt boride. The Tafel plots illustrated in Figure 3b indicate a similar performance trend as the CV measurements. The lowest Tafel slopes can be found for the $(Co_{1-x}Ni_x)_2B$ catalyst with $0 \leq x \leq 0.2$. The slopes of Co_2B and $(Co_{0.9}Ni_{0.1})_2B$ are around 60–80 mV dec^{-1}, while the two lowest slopes can be found for $(Co_{0.8}Ni_{0.2})_2B$ and surprisingly for $(Co_{0.5}Ni_{0.5})_2B$, which showed only an average performance in the CV curve activity. The low Tafel slope of $(Co_{0.5}Ni_{0.5})_2B$ could be explained by a change in the OER mechanism due to the high amount of nickel inside the catalyst phase. The $(Co_{0.7}Ni_{0.3})_2B$ and $(Co_{0.6}Ni_{0.4})_2B$ catalyst phases show the highest overpotential and with 82 mV dec^{-1} and 83 mV dec^{-1} the highest Tafel slopes. Since the Helmholtz double layer capacities C_{dl} values of the $(Co_{1-x}Ni_x)_2B$ catalysts vary by a factor of up to ≈ 3, a normalization of the different C_{dl} values to the lowest ($C_{dl} = 1.13$ mF cm^{-2}) one of the $(Co_{0.6}Ni_{0.4})_2B$ phase was performed (Figure 4a). Accordingly, we normalized the current densities of the CV curves of Figure 3a by normalization factors, which are their C_{dl} values divided by the lowest capacity of $(Co_{0.6}Ni_{0.4})_2B$. The resulting CV curve is shown in Figure 4b. The catalyst with the best catalytic performance $(Co_{0.9}Ni_{0.1})_2B$ remains the most active one strengthens its superiority to the second-best phase $(Co_{0.8}Ni_{0.2})_2B$. Consequently, it can be stated that the incorporation of a certain small amount of nickel into the binary cobalt boride phase increases the electrochemical activity independent of the different surface areas.

© 2021 The Authors. ChemCatChem published by Wiley-VCH GmbH

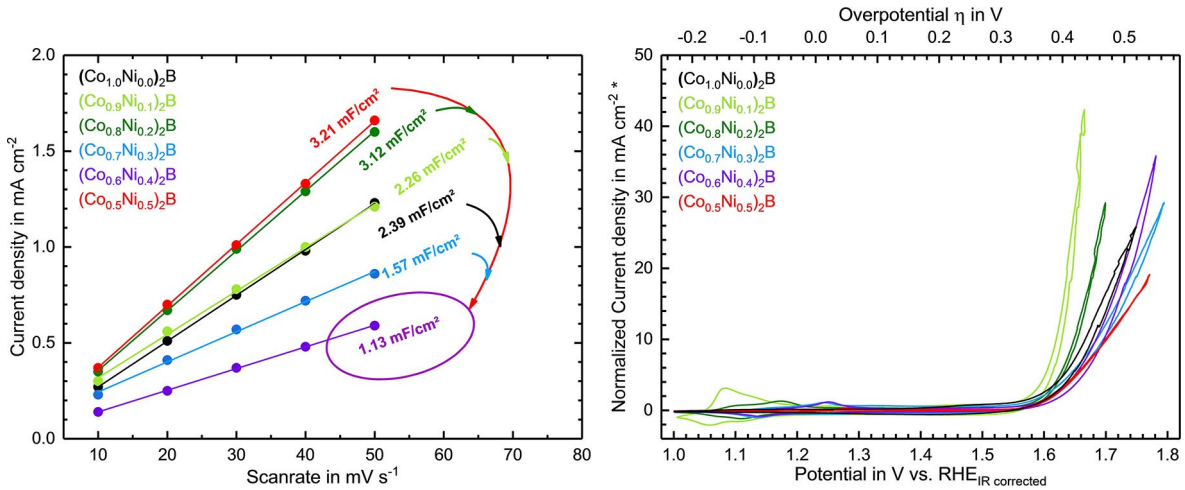

Figure 4. Fast sweep curves of Figure 3d marked with the lowest ECSA of $(Co_{0.6}Ni_{0.4})_2B$ in violet (left) and cyclic voltammetry measurements of Figure 3a *normalized on the smallest ECSA of $(Co_{0.6}Ni_{0.4})_2B$ (right).

The synergy between two or more transition metals is well known in literature. Mixed-metal catalysts, e.g. Co–Fe-based,[7,13,22,25,59,60] Ni–Fe-based[7,25,26,59,61–63] or Co–Ni-based[7,45,59,64–67] have been investigated before. In most of these studies, the mixture of the transition metals enhanced the electrochemical performance in comparison to the mono-metallic phase. These effects are not well understood so far, but they have been found amongst others in oxide/hydroxides,[26,61,64–66] phosphides,[68,69] and borides.[11,13,14,45,59,67] A summary of comparative overpotential values for other mixed-metal-borides can be found in the SI (see Table S3). In addition to the electrochemical activity, the stability of a catalyst is crucial for its technological application. Therefore, the long-term performance of the most active catalyst $(Co_{0.9}Ni_{0.1})_2B$ was investigated exemplarily by using a galvanostatic scan (GSS) at a constant current density of 10 mA cm^{-2} in 1 M KOH solution (Figure 3c). The catalyst was stable over the whole eight hours of measurement time at an overpotential of $\eta = 351$ mV. After the stability measurement, an additional CV curve (Figure 3c inset) was measured, showing an improvement in the overpotential ($\eta = 355$ mV at 10 mA cm^{-2}) compared to the catalytic performance of the catalyst before the GSS ($\eta = 371$ mV at 10 mA cm^{-2}). To understand these changes in the catalytic performance, detailed XPS measurements of the catalyst and F-AAS measurements of the electrolyte after different electrochemical measurement stages were conducted.

XPS surface analysis after electrochemical investigation

Further XPS analysis measurements of the surface of the most active $(Co_{0.9}Ni_{0.1})_2B$ catalyst were performed after the electrochemical activation procedure and after the whole electrochemical testing, in order to investigate changes introduced during these procedures and to identify the composition of the catalytically active species at the surface. The Ni 2p photoemission lines of $(Co_{0.9}Ni_{0.1})_2B$ after the activation (green) and after the electrochemical investigation (dark green) are shown in Figure 2c. The EC activation procedure strongly influenced the Ni 2p photoemission line (green) of the catalyst. The former nickel boride signal was barely visible anymore. However, two clearly noticeable signals for Ni 2p$^{3/2}$ arose at binding energies around 855.3 eV and 861.2 eV, which can be attributed to $Ni(OH)_2$ with its corresponding shake up peak.[50,51] After the EC investigation (dark green) the peak positions of the Ni 2p spectrum remained unchanged, but the intensity of the Ni 2p shake up peak exceeded the intensity of the Ni 2p$^{3/2}$ signal. This phenomenon cannot simply be clarified by the nickel photoemission line itself. In the survey spectra of the two samples (see SI; Figure S5) a higher Nafion signal and therefore higher fluorine content on the surface can be observed. This phenomenon could be due to different XPS measurement spots on the sample. The F KLL Auger structure of Nafion overlaps with the Ni 2p photoemission line (see SI; Figure S5) and therefore the signal at 861.2 eV shows a higher intensity than the Ni 2p$^{3/2}$ signal. In the XP Ni 2p detail spectrum of $(Co_{0.9}Ni_{0.1})_2B$ after the EC investigation (see SI; Figure S6) the F KLL Auger peak structure is fitted and subtracted from the measured signal, resulting in the residual Ni 2p photoemission line. The peak shape and position of the remaining Ni 2p signal confirms the assumption that nickel remained in its Ni^{2+} oxidation state as in $Ni(OH)_2$ after the EC investigation.[50,51] The Co 2p photoemission lines of $(Co_{0.9}Ni_{0.1})_2B$ after the activation (green) and after the whole electrochemical investigation (dark green) are shown in Figure 2a. After the activation procedure, the original Co_2B peak is no longer visible and is replaced by a strong feature at around 779.7 eV with an asymmetric peak shape, showing a shoulder part at around 780.8 eV, which can be assigned to a cobalt oxide or hydroxide component, respectively.[40–42] A satellite peak is visible at around 789.7 eV, leading to a distance between the Co 2p$^{3/2}$ photoemission line and the satellite of around 10 eV. In contrast to the Co^0-boride and $Co(OH)_2$ before the EC testing, the oxidation state of cobalt can now be identified as Co^{3+}.[40–42] Due to the fact, that the O 1s photo-

© 2021 The Authors. ChemCatChem published by Wiley-VCH GmbH

emission line (Figure 2d) shows the characteristics of metal-to-oxygen bonding at 529.1 eV as well as metal-to-hydroxide bonding at 530.9 eV, the cobalt phase that was present after the activation procedure was identified being cobalt oxyhydroxide ($Co^{3+}OOH$), which was observed in cobalt-based catalysts before.[10,13,22,25,70–72] In CoOOH the oxide and hydroxide characteristics in the O 1s photoemission line should be of similar intensity, according to the bonding ratio.[40,41,70,73] Here, the hydroxide species showed a slightly higher intensity compared to the oxide species, which can be explained by the presence of nickel hydroxide. After the EC investigation of $(Co_{0.9}Ni_{0.1})_2B$ the Co 2p photoemission line showed no further changes in the spectrum. Therefore, it can be stated that during the EC activation process the cobalt phase is already fully oxidized to $Co^{3+}OOH$. Hence, the cobalt, as well as the nickel phase, shows no further transformation after the EC activation process. The changes in the O 1s photoemission line after the EC investigation (Figure 2d) are due to the increased Nafion content of the spot analyzed by XPS, in which sulfonyl hydroxide ($R–S(=O)_2(OH)$), oxocarbon (CO_x) and oxocarbon with fluorine (OCF) components are accountable for the signals around 531.7–535 eV.[74,75] the electrochemical activation procedure the B 1s photoemission line (Figure 2b) vanished completely, which was already indicated from the Co 2p and Ni 2p photoemission lines, showing no remaining Co^0 and Ni^0 components associated with the boride in the spectra.[38,39,47–49] From a quantitative analysis of the discussed XP detail spectra (Table 1) of the different investigation stages it was found that the nickel-to-cobalt ratio increased with consecutive electrochemical testing. The nickel-to-cobalt ratio before EC testing was found to be 0.16. After the electrochemical activation, a ratio of 0.27 was calculated and the ratio after the complete EC testing was estimated to be 0.38. These finding could either be due to a degradation of the cobalt phase into the electrolyte or due to rearrangement of the surface phase during electrochemical treatment. To investigate either of these prospects, flame atomic absorption spectroscopy measurements of the alkaline electrolyte were used for the electrochemical testing of the catalyst after different measurement stages: before EC, after EC activation and after EC investigation. The F-AAS measurements were performed to analyze the cobalt as well as the nickel content in the electrolyte and are plotted in Figure 5.

The cobalt content (red) showed no change during the EC investigations, which led to the conclusion that no cobalt was degrading from the catalyst into the electrolyte. However, a change in the nickel content (black) of the electrolyte was found during the EC measurement procedure. Already after the EC activation, the nickel content decreased, showing after the EC investigation a total nickel mass loss in the electrolyte of 0.2 mg L^{-1}. If we consider that the complete loss in nickel content within the electrolyte is absorbed into the surface of the catalyst, an increased amount of the total catalyst composition can be calculated. The volume of the electrolyte inside the EC Zahner cell is limited to 7.2 mL, while the investigated surface is defined by an O-ring with a diameter of 0.5 cm. Hence, the size of the investigated area of the catalyst was calculated to be roughly 0.2 cm^2 ($A_{circle} = \pi\ r^2$). Due to a

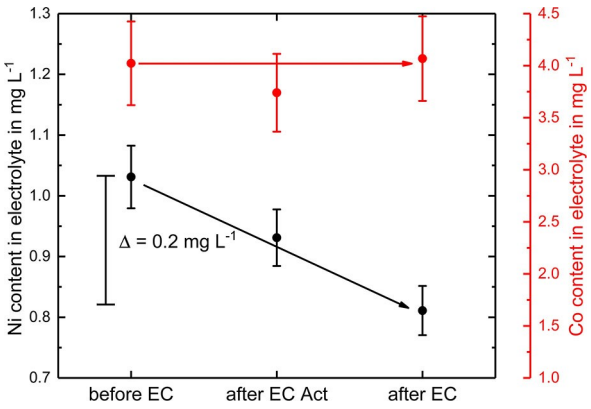

Figure 5. Flame atomic absorption spectroscopy measurements for the elements cobalt and nickel of the 1 M KOH electrolyte at the different measurement stages: as is, after EC activation (after EC act), after EC investigation (after EC).

total loading of 150 µg cm^{-2}, the loading of the investigated area was estimated to be 30 µg. The mass of adsorbed nickel from the electrolyte onto the surface was calculated with Equation (1), considering a homogenous adsorption.

$$\Delta Ni_{mass\ adsorbed} = \frac{0.2\ mg\ L^{-1}}{1000} \cdot 7.2\ mL \tag{1}$$

$$\Rightarrow \Delta Ni_{mass\ adsorbed} = 1.44\ \mu g$$

This led to an increase in the metallic mass of the whole catalyst loading of 5% and to an even higher percentage change with respect to the catalysts surface. Therefore, it can be stated that the change in nickel content found by XPS after the EC testing is due to nickel (re)adsorption from the electrolyte onto the surface of the catalyst during the EC investigation. This could explain the improved performance of the catalyst after the stability measurement. Similar findings concerning iron impurities found after electrochemical investigation of transition metal based catalysts in alkaline media, have been discussed in literature.[76] They are assumed to be responsible for an improved catalytic behavior of Ni-based catalysts in alkaline media.[26,61,62,76] A similar adsorption of iron from the alkaline electrolyte into the catalyst phase is unlikely, but cannot be entirely excluded. However, the nickel amount found by XPS is drastically increased after the EC treatment, while no iron can be found on the surface with XPS. A thick oxidation or rather hydroxylation layer is formed during the EC testing, leading to the active surface species of CoOOH and $Ni(OH)_2$. Equivalent metal oxyhydroxide active surface species have been proposed earlier for metal boride particles[31] and were found in boride catalysts tested for OER.[10,13,21,45]

Conclusion

We have identified an efficient and stable transition metal electrocatalyst for the OER in alkaline media. The preparation of

© 2021 The Authors. ChemCatChem published by Wiley-VCH GmbH

the mixed-metal borides was adapted from previous studies and followed a bottom-up synthesis technique at low temperature, followed by an annealing step at moderate temperature.[13] By this route highly reactive, crystalline powders of metal borides are formed. The powders were deposited using a standard drop coating technique on glassy carbon substrates. The OER active species was obtained from $(Co_{1-x}Ni_x)_2B$ by an electrochemical activation step in 1 M KOH and its main surface species were identified to be CoOOH and $Ni(OH)_2$. The best electrocatalytic activity is achieved by $(Co_{0.9}Ni_{0.1})_2B$, which is higher than that of the active phase of monometallic Co_2B, but in contrast to previous studies of the incorporation of iron into nanoscale dicobalt boride,[13] no drastic improvements on the onset potential were observed. The appearance of a second crystalline phase (Ni_3B) may obscure the peak performance point due to a restricted incorporation of nickel into the Co_2B structure under these synthesis conditions. During the electrochemical activation, the surface on the catalyst is oxidized, forming a metal (oxy-)hydroxide active surface species with CoOOH and $Ni(OH)_2$ evidently surrounding the Co–Ni boride bulk. The surface composition resembles phases found on mixed-metal oxides/hydroxides, while the bulk of the mixed metal boride contributes to a better electrical conductivity.[5,30] The cycling of the catalyst inside the electrolyte leads to an enhancement of the catalytic performance. By a combination of AAS and XPS measurements, we showed that nickel surface content is increased by a galvanic deposition/intercalation from the electrolyte onto/into the catalyst phase. This work provides detailed information on the surface modification mixed-metal-boride-based OER catalyst systems, while indicating the high significance of reaction processes that happen during the water oxidation in alkaline electrolytes. These processes cover electrochemical redox reactions of the catalyst itself and additionally reactions with impurities inside the electrolyte, strongly influencing the overall catalytic performance.

Acknowledgements

TEM measurements were performed by A. Zintler at the Advanced Electron Microscopy group (Prof. Molina-Luna, TU Darmstadt). Financial support by the DFG in the framework of the Darmstadt Graduate School of Excellence for Energy Science and Engineering (GSC 1070) and the project PAK 981 as well as by the BMBF (Mangan 03EK3552) is gratefully acknowledged. Open access funding enabled and organized by Projekt DEAL.

Conflict of Interest

The authors declare no conflict of interest.

[1] G. Akopov, M. T. Yeung, R. B. Kaner, *Adv. Mater.* **2017**, *29*, 1604506.
[2] B. Albert, H. Hillebrecht, *Angew. Chem. Int. Ed.* **2009**, *48*, 8640.
[3] Boniface P. T. Fokwa, in *Encycl. Inorg. Bioinorg. Chem.*, John Wiley & Sons Ltd, **2014**, pp. 1–14.
[4] B. Albert, K. Hofmann, *Metal Borides in Handbook of Solid State Chemistry, Materials and Structure of Solids (Vol.1)*, **2017**.
[5] S. Carenco, D. Portehault, C. Boissière, N. Mézailles, C. Sanchez, *Chem. Rev.* **2013**, *113*, 7981.
[6] B. Ganem, J. O. Osby, *Chem. Rev.* **1986**, *86*, 763.
[7] S. Gupta, M. K. Patel, A. Miotello, N. Patel, *Adv. Funct. Mater.* **2020**, *30*, DOI 10.1002/adfm.201906481.
[8] T. Osaka, H. Ishibashi, T. Endo, T. Yoshida, *Electrochim. Acta* **1980**, *26*, 339.
[9] T. Osaka, Y. Iwase, H. Kitayama, T. Ichino, *Chem. Soc. japan* **1983**, *56*, 2106.
[10] J. Masa, P. Weide, D. Peeters, I. Sinev, W. Xia, Z. Sun, C. Somsen, M. Muhler, W. Schuhmann, *Adv. Energy Mater.* **2016**, *6*, 1.
[11] J. Zhang, X. Li, Y. Liu, Z. Zeng, X. Cheng, Y. Wang, W. Tu, M. Pan, *Nanoscale* **2018**, *10*, 11997.
[12] J. M. V. Nsanzimana, Y. Peng, Y. Y. Xu, L. Thia, C. Wang, B. Y. Xia, X. Wang, *Adv. Energy Mater.* **2018**, *8*, 1.
[13] S. Klemenz, J. Schuch, S. Hawel, A. M. Zieschang, B. Kaiser, W. Jaegermann, B. Albert, *ChemSusChem* **2018**, *11*, 3150.
[14] S. Wang, P. He, Z. Xie, L. Jia, M. He, X. Zhang, F. Dong, H. Liu, Y. Zhang, C. Li, *Electrochim. Acta* **2019**, *296*, 644.
[15] J. M. V. Nsanzimana, L. Gong, R. Dangol, V. Reddu, V. Jose, B. Y. Xia, Q. Yan, J. M. Lee, X. Wang, *Adv. Energy Mater.* **2019**, *1901503*, 1.
[16] A. M. Zieschang, J. D. Bocarsly, J. Schuch, C. V. Reichel, B. Kaiser, W. Jaegermann, R. Seshadri, B. Albert, *Inorg. Chem.* **2019**, *58*, 16609.
[17] H. Chen, S. Ouyang, M. Zhao, Y. Li, J. Ye, *ACS Appl. Mater. Interfaces* **2017**, *9*, 40333.
[18] H. Li, P. Wen, Q. Li, C. Dun, J. Xing, C. Lu, S. Adhikari, L. Jiang, D. L. Carroll, S. M. Geyer, *Adv. Energy Mater.* **2017**, *7*, 1.
[19] J. M. V. Nsanzimana, R. Dangol, V. Reddu, S. Duo, Y. Peng, K. N. Dinh, Z. Huang, Q. Yan, X. Wang, *ACS Appl. Mater. Interfaces* **2019**, *11*, 846.
[20] J. Jiang, A. Zhang, L. Li, L. Ai, *J. Power Sources* **2015**, *278*, 445.
[21] J. Masa, C. Andronescu, H. Antoni, I. Sinev, S. Seisel, K. Elumeeva, S. Barwe, S. Marti-Sanchez, J. Arbiol, B. Roldan Cuenya, M. Muhler, W. Schuhmann, *ChemElectroChem* **2019**, *6*, 235.
[22] M. S. Burke, M. G. Kast, L. Trotochaud, A. M. Smith, S. W. Boettcher, *J. Am. Chem. Soc.* **2015**, *137*, 3638.
[23] L. J. Enman, M. S. Burke, A. S. Batchellor, S. W. Boettcher, *ACS Catal.* **2016**, *6*, 2416.
[24] A. M. Smith, L. Trotochaud, M. S. Burke, S. W. Boettcher, *Chem. Commun.* **2015**, *51*, 5261.
[25] M. S. Burke, S. Zou, L. J. Enman, J. E. Kellon, C. A. Gabor, E. Pledger, S. W. Boettcher, *J. Phys. Chem. Lett.* **2015**, *6*, 3737.
[26] L. Trotochaud, J. K. Ranney, K. N. Williams, S. W. Boettcher, *J. Am. Chem. Soc.* **2012**, *134*, 17253.
[27] N. B. Halck, V. Petrykin, P. Krtil, J. Rossmeisl, *Phys. Chem. Chem. Phys.* **2014**, *16*, 13682.
[28] D. Friebel, M. W. Louie, M. Bajdich, K. E. Sanwald, Y. Cai, A. M. Wise, M. J. Cheng, D. Sokaras, T. C. Weng, R. Alonso-Mori, R. C. Davis, J. R. Bargar, J. K. Nørskov, A. Nilsson, A. T. Bell, *J. Am. Chem. Soc.* **2015**, *137*, 1305.
[29] Y. Li, P. Hasin, Y. Wu, *Adv. Mater.* **2010**, *22*, 1926.
[30] C. C. Wang, S. A. Akbar, W. Chen, V. D. Patton, *J. Mater. Sci.* **1995**, *30*, 1627.
[31] G. P. Shveikin, A. L. Ivanovskii, *Russ. Chem. Rev.* **1994**, *63*, 711.
[32] D. A. Shirley, *Phys. Rev. B* **1972**, *5*, 4709.
[33] K. H. J. Buschow, P. G. van Engen, R. Jongebreur, *J. Magn. Magn. Mater.* **1983**, *38*, 1.
[34] B. C. Chakoumakos, M. Paranthaman, *Phys. C Supercond. its Appl.* **1994**, *227*, 143.
[35] C. Kapfenberger, B. Albert, R. Pöttgen, H. Huppertz, *Zeitschrift für Krist.* **2006**, *221*, 477.
[36] S. Trasatti, O. A. Petrii, *Pure Appl. Chem.* **1991**, *63*, 711.
[37] C. Wei, S. Sun, D. Mandler, X. Wang, S. Z. Qiao, Z. J. Xu, *Chem. Soc. Rev.* **2019**, *48*, 2518.
[38] G. Mavel, J. Escard, P. Costa, J. Castaing, *Surf. Sci.* **1973**, *35*, 109.
[39] P. Krishnan, K. L. Hsueh, S. D. Yim, *Appl. Catal. B* **2007**, *77*, 206.
[40] M. Oku, K. Hirokawa, *J. Electron Spectrosc. Relat. Phenom.* **1976**, *8*, 475.
[41] J. Yang, H. Liu, W. N. Martens, R. L. Frost, *J. Phys. Chem. C* **2010**, *114*, 111.
[42] M. C. Biesinger, B. P. Payne, A. P. Grosvenor, L. W. M. Lau, A. R. Gerson, R. S. C. Smart, *Appl. Surf. Sci.* **2011**, *257*, 2717.
[43] K. Elumeeva, J. Masa, D. Medina, E. Ventosa, S. Seisel, Y. U. Kayran, A. Genç, T. Bobrowski, P. Weide, J. Arbiol, M. Muhler, W. Schuhmann, *J. Mater. Chem. A* **2017**, *5*, 21122.
[44] P. Chen, K. Xu, T. Zhou, Y. Tong, J. Wu, H. Cheng, X. Lu, H. Ding, C. Wu, Y. Xie, *Angew. Chem. Int. Ed.* **2016**, *55*, 2488.

© 2021 The Authors. ChemCatChem published by Wiley-VCH GmbH

[45] N. Xu, G. Cao, Z. Chen, Q. Kang, H. Dai, P. Wang, *J. Mater. Chem. A* **2017**, *5*, 12379.
[46] C. Zhu, D. Wen, S. Leubner, M. Oschatz, W. Liu, M. Holzschuh, F. Simon, S. Kaskel, A. Eychmüller, *Chem. Commun.* **2015**, *51*, 7851.
[47] Y. Okamoto, Y. Nitta, T. Imanaka, S. Teranishi, *J. Chem. Soc. Faraday Trans. 1 Phys. Chem. Condens. Phases* **1979**, *75*, 2027.
[48] J. A. Schreifels, P. C. Maybury, W. E. Swartz, *J. Catal.* **1980**, *65*, 195.
[49] J. Legrand, A. Taleb, S. Gota, M. J. Guittet, C. Petit, *Langmuir* **2002**, *18*, 4131.
[50] B. P. Payne, M. C. Biesinger, N. S. McIntyre, *J. Electron Spectrosc. Relat. Phenom.* **2012**, *185*, 159.
[51] R. S. C. Smart, A. P. Grosvenor, M. C. Biesinger, N. S. McIntyre, *Surf. Sci.* **2006**, *600*, 1771.
[52] J. H. Scofield, *J. Electron Spectrosc. Relat. Phenom.* **1976**, *8*, 129.
[53] Y. Wang, J. Fan, M. Trenary, *Chem. Mater.* **1993**, *5*, 192.
[54] Y. Wang, M. Trenary, *Chem. Mater.* **1993**, *5*, 199.
[55] C. W. Ong, H. Huang, B. Zheng, R. W. M. Kwok, Y. Y. Hui, W. M. Lau, *J. Appl. Phys.* **2004**, *95*, 3527.
[56] O. M. Moon, B. C. Kang, S. B. Lee, J. H. Boo, *Thin Solid Films* **2004**, *464–465*, 164.
[57] E. McCafferty, J. P. Wightman, E. Mcca, J. P. Wightman, *Surf. Interface Anal.* **1998**, *26*, 549.
[58] R. L. Doyle, I. J. Godwin, M. P. Brandon, M. E. G. G. Lyons, *Phys. Chem. Chem. Phys.* **2013**, *15*, 13737.
[59] Y. Li, B. Huang, Y. Sun, M. Luo, Y. Yang, Y. Qin, L. Wang, C. Li, F. Lv, W. Zhang, S. Guo, *Small* **2019**, *15*, 1.
[60] C. Xiao, X. Lu, C. Zhao, *Chem. Commun.* **2014**, *50*, 10122.
[61] L. Trotochaud, S. L. Young, J. K. Ranney, S. W. Boettcher, *J. Am. Chem. Soc.* **2014**, *136*, 6744.
[62] J. R. Swierk, S. Klaus, L. Trotochaud, A. T. Bell, T. D. Tilley, *J. Phys. Chem. C* **2015**, *119*, 19022.
[63] J. M. V. Nsanzimana, V. Reddu, Y. Peng, Z. Huang, C. Wang, X. Wang, *Chem. A Eur. J.* **2018**, *24*, 18502.
[64] L. K. Wu, W. Y. Wu, J. Xia, H. Z. Cao, G. Y. Hou, Y. P. Tang, G. Q. Zheng, *J. Mater. Chem. A* **2017**, *5*, 10669.
[65] L. K. Wu, W. Y. Wu, J. Xia, H. Z. Cao, G. Y. Hou, Y. P. Tang, G. Q. Zheng, *Electrochim. Acta* **2017**, *254*, 337.
[66] L. K. Wu, J. Xia, H. Z. Cao, Y. P. Tang, G. Y. Hou, G. Q. Zheng, *Int. J. Hydrogen Energy* **2017**, *42*, 10813.
[67] H. S. Han, Y. R. Hong, J. Woo, S. Mhin, K. M. Kim, J. Kwon, H. Choi, Y. C. Chung, T. Song, *Adv. Energy Mater.* **2019**, *1803799*, 1.
[68] B. Qiu, L. Cai, Y. Wang, Z. Lin, Y. Zuo, M. Wang, Y. Chai, *Adv. Funct. Mater.* **2018**, *28*, 1.
[69] A. Mendoza-Garcia, D. Su, S. Sun, *Nanoscale* **2016**, *8*, 3244.
[70] N. Weidler, S. Paulus, J. Schuch, J. Klett, S. Hoch, P. Stenner, A. Maljusch, J. Brötz, C. Wittich, B. Kaiser, W. Jaegermann, *Phys. Chem. Chem. Phys.* **2016**, *18*, 10708.
[71] R. Subbaraman, D. Tripkovic, K. C. Chang, D. Strmcnik, A. P. Paulikas, P. Hirunsit, M. Chan, J. Greeley, V. Stamenkovic, N. M. Markovic, *Nat. Mater.* **2012**, *11*, 550.
[72] L. Trotochaud, S. W. Boettcher, *Scr. Mater.* **2014**, *74*, 25.
[73] N. S. Mcintyre, M. G. Cook, *Anal. Chem.* **1975**, *47*, 2208.
[74] C. Chen, G. Levitin, D. W. Hess, T. F. Fuller, *J. Power Sources* **2007**, *169*, 288.
[75] A. K. Friedman, W. Shi, Y. Losovyj, A. R. Siedle, L. A. Baker, *J. Electrochem. Soc.* **2018**, *165*, H733.
[76] D. A. Corrigan, *J. Electrochem. Soc.* **1987**, *134*, 377.

Manuscript received: December 22, 2020
Revised manuscript received: February 8, 2021
Accepted manuscript online: February 22, 2021
Version of record online: March 19, 2021

© 2021 The Authors. ChemCatChem published by Wiley-VCH GmbH